Article

The CRL4[DCAF1] cullin-RING ubiquitin ligase is activated following a switch in oligomerization state

Weaam I Mohamed[1,2,†] (iD), Andreas D Schenk[1] (iD), Georg Kempf[1] (iD), Simone Cavadini[1] (iD), Anja Basters[1] (iD), Alessandro Potenza[1,2], Wassim Abdul Rahman[1], Julius Rabl[1,†] (iD), Kurt Reichermeier[3,4] (iD) & Nicolas H Thomä[1,*] (iD)

Abstract

The cullin-4-based RING-type (CRL4) family of E3 ubiquitin ligases functions together with dedicated substrate receptors. Out of the ~29 CRL4 substrate receptors reported, the DDB1- and CUL4-associated factor 1 (DCAF1) is essential for cellular survival and growth, and its deregulation has been implicated in tumorigenesis. We carried out biochemical and structural studies to examine the structure and mechanism of the CRL4[DCAF1] ligase. In the 8.4 Å cryo-EM map of CRL4[DCAF1], four CUL4-RBX1-DDB1-DCAF1 protomers are organized into two dimeric sub-assemblies. In this arrangement, the WD40 domain of DCAF1 mediates binding with the cullin C-terminal domain (CTD) and the RBX1 subunit of a neighboring CRL4[DCAF1] protomer. This renders RBX1, the catalytic subunit of the ligase, inaccessible to the E2 ubiquitin-conjugating enzymes. Upon CRL4[DCAF1] activation by neddylation, the interaction between the cullin CTD and the neighboring DCAF1 protomer is broken, and the complex assumes an active dimeric conformation. Accordingly, a tetramerization-deficient CRL4[DCAF1] mutant has higher ubiquitin ligase activity compared to the wild-type. This study identifies a novel mechanism by which unneddylated and substrate-free CUL4 ligases can be maintained in an inactive state.

Introduction

DCAF1 is an essential substrate receptor for the cullin 4 RING ubiquitin E3 ligase (CRL4) family. DCAF1 is implicated in fundamental cellular processes, ranging from DNA replication (McCall *et al*, 2008), cell cycle progression (McCall *et al*, 2008; Guo *et al*, 2016), transcription (Wang *et al*, 2017), to zygotic development and reproduction (Yu *et al*, 2013). CRL4[DCAF1] (CUL4-DDB1-RBX1-DCAF1) activity requires the direct interaction between the DCAF1 substrate receptor and various reported substrates such as the replication factor MCM10 (Kaur *et al*, 2012), p53 (Hrecka *et al*, 2007; Guo *et al*, 2016), FoxM1 (Wang *et al*, 2017), TET methylcytosine dioxygenases (Yu *et al*, 2013), and protein phosphatase 2A (Yu *et al*, 2015). DCAF1 is conserved among metazoans and is ubiquitously expressed in different tissues (Zhang *et al*, 2001). Loss of DCAF1 in mice leads to early embryonic lethality (McCall *et al*, 2008). DCAF1 ablation is often associated with defects in cell cycle, cell division, and cell survival (Schabla *et al*, 2019). A comprehensive high-throughput RNAi screening study in ~400 different cell lines found that loss of DCAF1 is pan-lethal (McDonald *et al*, 2017), with DCAF1 knock-down induced lethality being the highest among all reported CUL4 DCAF substrate receptors in the study (Fig EV1A). CRL4[DCAF1] is also the second most abundant CRL4 complex, accounting for ~12% of all assembled CRL4 complexes, rendering DCAF1 a critical substrate receptor for the CRL4 system (Reichermeier *et al*, 2020).

The CRL4[DCAF1] E3 ligase is frequently hijacked by viruses such as the human immunodeficiency virus type 1 and 2 (HIV-1, HIV-2) and their viral accessory proteins VPR and VPX (Romani & Cohen, 2012). Efficient replication of HIV in macrophages requires the interaction of VPR/VPX with DCAF1 (Kyei *et al*, 2015), which redirects the CRL4[DCAF1] ubiquitin ligase activity toward degradation of host proteins such as UNG2 (Wu *et al*, 2016) and SAMHD1 (Schwefel *et al*, 2014). Viral-induced degradation of host proteins via

1 Friedrich Miescher Institute for Biomedical Research, Basel, Switzerland
2 University of Basel, Basel, Switzerland
3 Division of Biology and Biological Engineering, California Institute of Technology, Pasadena, CA, USA
4 Genentech, South San Francisco, CA, USA
   *Corresponding author. Tel: +41 61 697 66 51; E-mail: nicolas.thoma@fmi.ch
   †Present address: ETH-Zürich, Zürich, Switzerland

CRL4[DCAF1] was shown to enhance HIV infection by facilitating viral replication and propagation (Baldauf *et al*, 2017).

Several lines of evidence further implicate DCAF1 in cancer progression. Hrecka *et al* (2007) reported that DCAF1 depletion stabilizes the expression of p53 and several of its target genes. Follow-up studies linked the role of DCAF1 to regulating p53 transcriptional activity in different cell types (Kim *et al*, 2012; Guo *et al*, 2016; Wang *et al*, 2016a). Recent work has also found that MERLIN, a protein that is commonly mutated in several glial cancers, mediates its tumor suppression activities *via* inactivation of CRL4[DCAF1] (Li *et al*, 2010, 2014).

Despite the growing interest in studying DCAF1 physiological functions, the molecular determinants of DCAF1 regulation are currently poorly understood. CRL systems share common modes of regulation including activation by the ubiquitin-like protein NEDD8 (neural precursor cell expressed, developmentally downregulated 8) (neddylation) (Duda *et al*, 2008), inactivation by the multisubunit deneddylase COP9 signalosome (CSN) (Lingaraju *et al*, 2014), and substrate receptor (SR) exchange mediated by CAND1 (Cullin-associated Nedd8-dissociated protein) (Pierce *et al*, 2013). Besides the standard CRL regulatory mechanisms, DCAF1 has been suggested to be governed by additional modes of activity control. For instance, MERLIN mediates direct binding to DCAF1 and has been linked to CRL4[DCAF1] ligase inhibition by an as yet undefined mechanism (Li *et al*, 2010). Moreover, DCAF1 is known to dimerize *in vivo* and *in vitro*, and dimerization is proposed to enhance CRL4[DCAF1] ubiquitination activity *in vitro* (Ahn *et al*, 2011). The SECexplorer workflow fractionates native protein complexes by size-exclusion chromatography (SEC) followed by mass spectrometry to identify proteins in each fraction, along with an apparent molecular weight for the eluting complexes (Heusel *et al*, 2019). The size-exclusion profile in SECexplorer finds DCAF1 eluting with large native protein complexes of more than 1 MDa.

In the current study, we have used protein biochemistry and cryo-electron microscopy (cryo-EM) to characterize the CRL4[DCAF1] complex *in vitro*. We obtained an 8.4 Å cryo-EM map of CRL4[DCAF1], which finds the complex in a tetrameric arrangement. In the tetrameric conformation the DCAF1 WD40 domain mediates the interaction with the cullin C-terminal domain (CTD) and RBX1 of a neighboring CRL4[DCAF1] protomer. This architecture renders the RING domain of RBX1 inaccessible for the E2 ubiquitin-conjugating enzyme. Upon activation of CRL4[DCAF1] by neddylation, the interaction between the cullin CTD and DCAF1 is disrupted and the complex becomes dimeric and active. This dimeric state is also induced when the viral proteins VPR-UNG2 are bound to CRL4[DCAF1], while the presence of MERLIN is compatible with the tetrameric autoinhibited state of the ligase. These results suggest a novel mechanism by which the activity of isolated CRL4[DCAF1] ligase is regulated by oligomerization.

Results

CRL4[DCAF1] exists in a dimer/tetramer equilibrium

The 1507 amino acid human DCAF1 receptor consists of a HLH (helix-loop-helix) and a WD40 domain at the C-terminus, which together mediate DDB1 binding (Fig 1A), and in turn bridges DCAF1

to the cullin scaffold (Fig EV1B). A highly acidic tail spans the very C-terminus of DCAF1, which is reported to mediate MERLIN and p53 binding (Mori *et al*, 2014; Wang *et al*, 2016a). The large N-terminal domain of DCAF1 is predicted to assume an Armadillo-like fold (Zimmermann *et al*, 2018). A Lis1 homology (LisH) motif spans residues 846–878 at the N-terminus and has been implicated in DCAF1 dimerization (Ahn *et al*, 2011).

To investigate the oligomeric state of CRL4[DCAF1], we first purified the wild-type CRL4[DCAF1] complex and performed a neddylation reaction to generate N8-CRL4[DCAF1] complex (Fig 1B). This was followed by multi-angle light scattering coupled with size-exclusion chromatography (SEC-MALS) on the neddylated (N8-CRL4[DCAF1]) and unneddylated (CRL4[DCAF1]) complexes. While the SEC-MALS analysis of the neddylated state of CRL4[DCAF1] gives a molecular weight (MW) consistent with a dimeric complex (observed MW 780 kDa, calculated MW 810 kDa), the unneddylated form of CRL4[DCAF1] has an estimated MW equivalent to a tetramer (observed MW 1,561 kDa, calculated MW 1,582 kDa) (Fig 1C). The polydispersity values (M_w/M_n) are 1.002 and 1.000, respectively, in line with these complexes being present as single, mono-disperse species (Fig 1C). These data suggest that CRL4[DCAF1] switches its oligomeric form as a function of neddylation state. SEC-MALS analysis on an N-terminally truncated mutant of CRL4[DCAF1(ΔNTD)] (987–1,507), lacking the LisH motif, finds a MW of 289 kDa, which corresponds to a monomeric complex with a MW of 287 kDa (Fig EV1C and D), linking the LisH motif in DCAF1 to dimerization (Ahn *et al*, 2011). SEC-MALS analysis on the isolated DDB1-DCAF1 (FL) shows this sub-complex elutes as a dimer (observed MW 563 kDa, calculated MW 592 kDa) (Fig EV1C and D), suggesting a role of the cullin-RBX1 scaffold in tetramer formation.

The RBX1 interaction with DCAF1 drives tetramer formation

To gain molecular insights into neddylation-dependent changes in the oligomeric state of CRL4[DCAF1], we pursued structural analysis by single particle cryo-EM. In an effort to increase the stability of CRL4[DCAF1] protein sample for freezing cryo-EM grids, we had to cross-link the sample using a gradient fixation protocol (GraFix) (Stark, 2010). This enabled us to obtain an 8.4 Å-resolution cryo-EM map of the unneddylated CRL4[DCAF1] complex (Fig EV2A–C). In the cryo-EM map, CRL4[DCAF1] assembles into a tetrameric arrangement (Fig 2A and B). Intrinsic flexibility between the protomers of this assembly likely prevented us from obtaining higher-resolution structural insight. The cryo-EM map was interpreted by rigid body and restrained flexible fitting of crystallographic models of CUL4-DDB1-RBX1 (PDB 2HYE), and DDB1-DCAF1 (WD40) (PDB 5JK7), which allowed defining the overall architecture of the assembly.

The CRL4[DCAF1] map indicates a potential intermolecular interaction between the DCAF1 (WD40) of one molecule, with the cullin C-terminal domain (CTD) and RBX1 of a neighboring protomer (Fig 3A). An elementary dimer formed by two CRL4[DCAF1] molecules is also evident in the map and is consistent with the interaction of two neighboring LisH domains located proximal to the WD40 domain (Fig EV3A). The tetrameric CRL4[DCAF1] assembly in our structure is thus comprised of two CRL4[DCAF1] dimers. The structural data are consistent with the results obtained by SEC-MALS, illustrating that CRL4[DCAF1] is tetrameric, and that tetramerization is mediated by the interactions of the cullin CTD-RBX1 and DCAF1 WD40
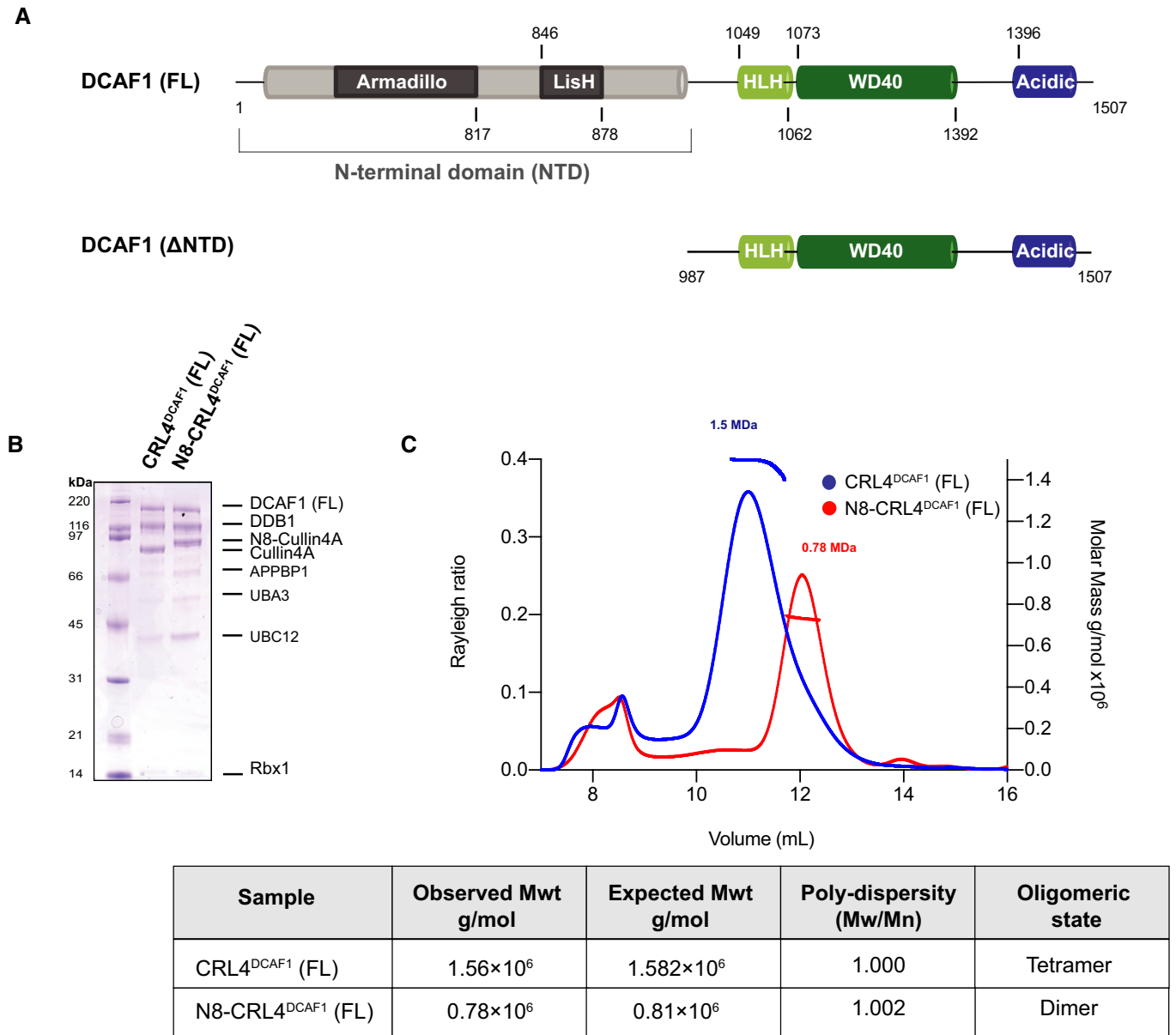
A

DCAF1 (FL)

846   1049 1073   1396

Armadillo   LisH   HLH+   WD40   Acidic

1   1507

817   878   1062   1392

N-terminal domain (NTD)

DCAF1 (ΔNTD)

HLH+   WD40   Acidic

987   1507

B

CRL4^DCAF1 (FL)
N8-CRL4^DCAF1 (FL)

kDa
220
116
97
— DCAF1 (FL)
— DDB1
— N8-Cullin4A
— Cullin4A
66
— APPBP1
— UBA3
45
— UBC12
31

21

14
— Rbx1

C

1.5 MDa

0.78 MDa

● CRL4^DCAF1 (FL)
● N8-CRL4^DCAF1 (FL)

Rayleigh ratio

Molar Mass g/mol x10^6

Volume (mL)

Sample	Observed Mwt g/mol	Expected Mwt g/mol	Poly-dispersity (Mw/Mn)	Oligomeric state
CRL4^DCAF1 (FL)	1.56×10^6	1.582×10^6	1.000	Tetramer
N8-CRL4^DCAF1 (FL)	0.78×10^6	0.81×10^6	1.002	Dimer

Figure 1. CRL4^DCAF1 exists in a dimer/tetramer equilibrium.

A   Predicted domain organization of the human DCAF1 (FL).
B   SDS–PAGE Coomassie gel of the neddylation reaction of CRL4^DCAF1 at time 0 h and the fully neddylated N8-CRL4^DCAF1 after 2 h.
C   SEC-MALS analysis of CRL4^DCAF1 and N8-CRL4^DCAF1. The chromatogram displays Rayleigh ratio curves for CRL4^DCAF1 (blue) and N8-CRL4^DCAF1 (red) together with the molar mass (MDa) of the main peaks calculated by MALS. The table summarizes the SEC-MALS observed molecular weights in the main peaks, the calculated molecular weights, polydispersity values, and oligomeric states of the tested complexes.

Source data are available online for this figure.

domain at one dimerization interface, and the DCAF1 N-terminal LisH motifs at the other.

Modeling of the DCAF1 Armadillo (ARM) and LisH domains

The putative LisH density proximal to the WD40 domain showed helical features and strongly suggested the presence of a two-fold symmetry axis in line with previously observed LisH domain homodimers (PDB 1UUJ, PDB 1VYH) (Kim *et al*, 2004; Tarricone *et al*, 2004). The LisH domain fold is characterized by a two-helix bundle (helices 1 and 2) with a third helix (helix 3) crossing the helical bundle (e.g. PDB 1UUJ, PDB 6IWV). Upon homodimerization, the two-helix bundles form a four-helix bundle in which helices 1 and 2 align in an anti-parallel and slightly diagonal manner, respectively. In several structures, helices 3 of the homodimeric assembly additionally align in a diagonal manner
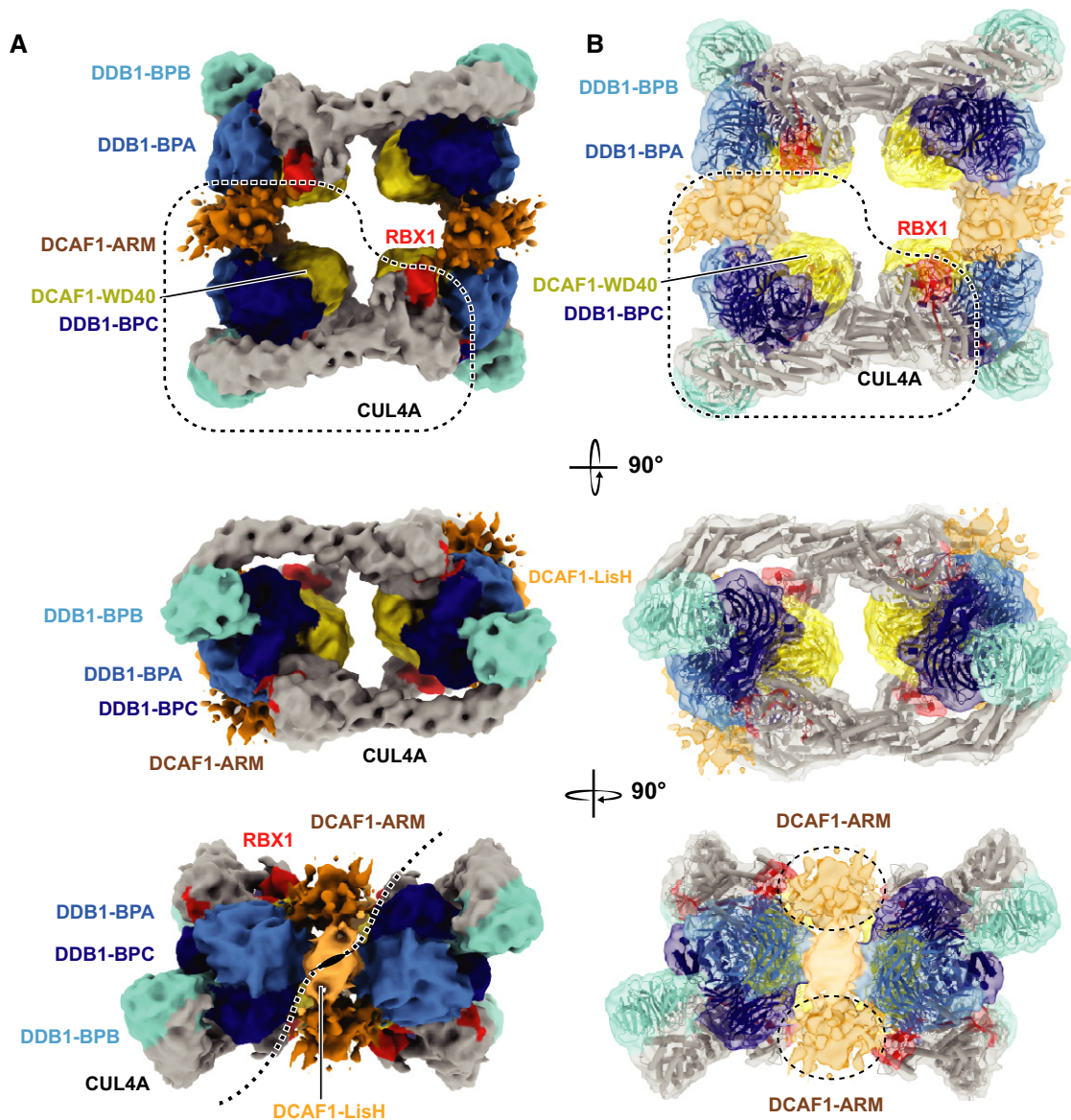
Figure 2. The CRL4^{DCAF1} assembles a tetrameric complex.

A, B   Different views of CRL4^{DCAF1} cryo-EM map (8.4 Å) with fitted crystal structures of CUL4A (gray), RBX1 (red) (PDB 2HYE), DDB1 BPA (light blue), BPB (cyan), and BPC (dark blue), DCAF1 WD40 domain (yellow) (PDB 5JK7), LisH domain (orange), and ARM domain (brown) in (A) surface representation, and (B) cartoon representation.

perpendicular to the four-helix bundle (PDB 1UUJ, PDB 6IWV). The DCAF1 LisH domain structure was predicted by comparative modeling with high confidence (confidence score of 0.67, Song *et al*, 2013). To obtain a model for the homodimeric complex, the monomeric consensus model from comparative modeling (aa 846–883) was superposed on the dimeric LisH domains from PDB 6IWV. The homodimer interface was independently validated by docking two separated LisH monomer models against each other, imposing twofold symmetry constraints (see Materials and Methods). In these simulations, the LisH dimer interface previously observed in homologous dimeric LisH crystal structures gave the best docking scores (Fig EV3B). The dimeric homology model (obtained from superposition on a template structure) was then docked into the putative LisH

density (Fig EV3A and C). The density supports an anti-parallel alignment of helices 2, while the putative density for helices 1 is fragmented. We observed only uninterpretable density at the expected location for helices 3 and refrained from modeling this helix given the limited local resolution.

A significant portion of uninterpreted density located between DDB1 BPA and DDB1 BPB of different protomers and close to the putative LisH density showed features indicative of several α-helical bundles. These features would be in agreement with an armadillo fold predicted for the segment N-terminal to the DCAF1 LisH domain (ARM, 1–817). To obtain a model for this part, we employed the deep learning-based structure prediction pipeline *Alphafold* that has been shown to yield highly accurate predictions

A

B

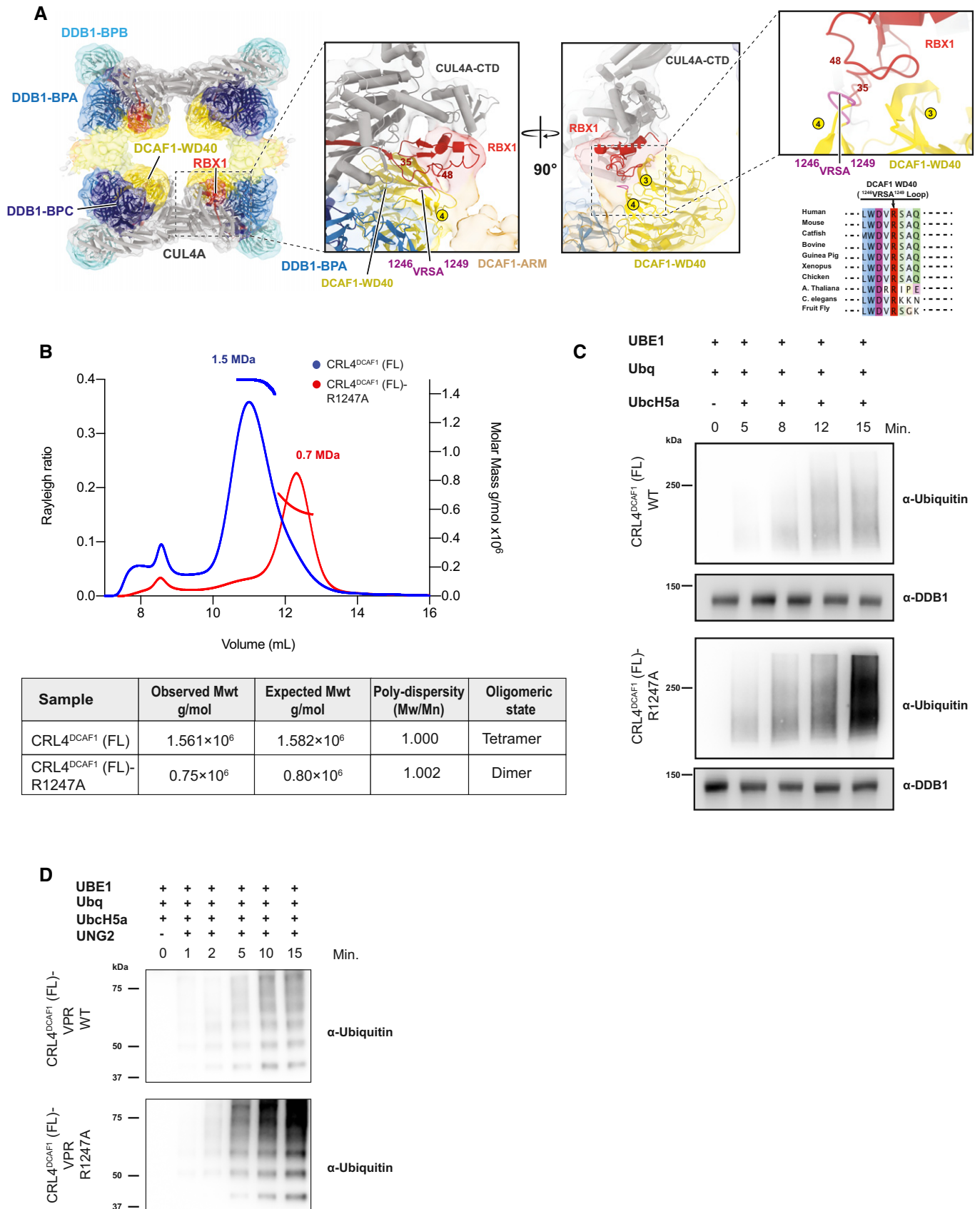| Sample	Observed Mwt g/mol	Expected Mwt g/mol	Poly-dispersity (Mw/Mn)	Oligomeric state
CRL4^DCAF1 (FL)	1.561×10^6	1.582×10^6	1.000	Tetramer
CRL4^DCAF1 (FL)-R1247A	0.75×10^6	0.80×10^6	1.002	Dimer

C

D

Figure 3.

Figure 3. The DCAF1 WD40 domain is essential for tetramer formation.

A   CRL4^{DCAF1} cryo-EM map (8.4 Å) with fitted model (left), and a close-up view of the CRL4^{DCAF1} map shows the interaction between DCAF1 (WD40) in yellow and RBX1 in red. The loop in DCAF1 (WD40) that contains the mutated arginine (R1247) is colored in violet. Circled numbers indicate the respective blades in the WD40 β-propeller. The RBX1 segment potentially contacting the VRSA loop in DCAF1 is indicated by flanking residue numbers. Conservation plot in the region around the residue R1247 in DCAF1 is shown to the lower right.

B   SEC-MALS analysis of CRL4^{DCAF1} and CRL4^{DCAF1} (R1247A) mutant. The chromatogram displays Rayleigh ratio curves of CRL4^{DCAF1} WT (blue) and mutant CRL4^{DCAF1} (R1247A) (red) together with the molar mass (MDa) of the main peaks calculated by MALS. The table summarizes the SEC-MALS observed molecular weights in the main peaks, the calculated molecular weight, polydispersity values, and oligomeric states of the tested complexes.

C   Autoubiquitination of DCAF1 by wild-type CRL4^{DCAF1} (FL) (top) or mutant CRL4^{DCAF1} (FL) (R1247A) (bottom) observed after incubation with UBA1, UbcH5a, Ubiquitin (WT), at 30°C for 0 to 15 min as indicated (n = 3).

D   Ubiquitination of UNG2 by wild-type CRL4^{DCAF1}-VPR (FL) (top) or mutant CRL4^{DCAF1}-VPR (FL) (R1247A) (bottom) observed after incubation with UBA1, UbcH5a, Ubiquitin (WT), at 30°C for 0 to 15 min as indicated (n = 3).

Source data are available online for this figure.

even in case of targets where no structural templates of close homologs are available (Fig EV3D; Jumper *et al*, 2021). The part directly N-terminal to the LisH domain (aa 507–817), which was approximately matching the volume of the remaining density, was extracted from the top-ranked model of *Alphafold*. In the predicted model, the extracted portion contains four complete armadillo (ARM) repeats each composed of a short helix that is perpendicular to two somewhat diagonal and anti-parallel aligned longer helices and an incomplete repeat (third helix only) at the N-terminus. This particular helix was predicted to be significantly longer. Due to the strong repetitiveness of the α-helical repeats and the poor map quality in this region, it was not possible to unambiguously dock the model and we cannot exclude that the observed density corresponds to a different part of the ARM domain. In Fig EV3A the three best fitting poses with real-space correlations between 0.52 and 0.59 (calculated with a simulated model-map at 8.4 Å) are shown.

In our fitted models, a gap of around 33–46 Å with uninterpretable density remained between the C-terminal part of the DCAF1 ARM domain and the DCAF1 LisH domain (Fig EV3A and C). These distances would be all consistent with the length of a linker region of 29 aa, which is predicted to be (partially) α-helical. Some ARM units are interspersed by loop regions and, in particular, the four C-terminal repeats are connected to the next N-terminal repeat by a region that has been previously suggested to contain a small chromo-like domain (Schabla *et al*, 2019). Owing to the limited local resolution, the presence of a chromo-like fold could not be verified. No density was observed for the remaining N-terminal part of the ARM domain that would be consistent with an interspersed casein-kinase like domain (Kim *et al*, 2013).

Overall, the density suggests the presence of a symmetric α-helical interaction motif and several armadillo-like repeats in close proximity that likely correspond to the LisH domain and the C-terminal part of the ARM domain, respectively. Predicted models for these regions of the map can largely explain the density features at the given resolution. Higher resolution experimental data are required to unambiguously dock a model and carry out more detailed residue assignments.

The DCAF1 WD40 domain is essential for tetramer formation

The subnanometer CRL4^{DCAF1} cryo-EM map allowed fitting of the DCAF1 WD40 and RBX1 domains into the four copies with reasonable confidence. Within the RBX1/DCAF1 region, we identified a highly conserved loop at the surface of the WD40 propeller that

approaches RBX1, namely, loop: ^{1246}VRSA^{1249} (Fig 3A). We introduced an alanine mutation at the conserved arginine residue 1247 within this loop, and analyzed the mutated CRL4^{DCAF1} complex by SEC-MALS. SEC-MALS analysis showed that this single mutation R1247A is sufficient to disassemble the tetrameric complex into a fully dimeric one (Fig 3B). These data support the model interpretation where the interaction between DCAF1 and the RBX1 RING domain is a key driver in tetramerization, and further confirms the assignment of the two elementary CRL4^{DCAF1} dimers that together form the tetramer.

The cryo-EM map finds the RBX1 RING domain shielded by the WD40 domain of DCAF1, rendering it inaccessible for an Ub-loaded E2 (Fig 3A). To test whether the tetrameric CRL4^{DCAF1} assembly represents an inactive autoinhibited state, we carried out auto-ubiquitination assays using the wild-type and R1247A mutant of CRL4^{DCAF1} (FL). The wild-type tetrameric CRL4^{DCAF1} complex shows a prominent reduction in DCAF1 auto-ubiquitination as compared to the dimeric mutant CRL4^{DCAF1} (R1247A) (Fig 3C). Reduced catalytic activity of the tetrameric CRL4^{DCAF1} compared to the dimeric mutant was also observed toward the viral substrate VPR-UNG2 (Fig 3D). On the other hand, preventing tetramer formation by incorporating the mutant DCAF1 (R1247A) into the complex overcomes auto-inhibition and gives rise to a more active E3 ligase (Fig 3C and D). Taken together, these data suggest that the tetrameric CRL4^{DCAF1} ligase represents a conformation with a significantly reduced catalytic activity.

Tetrameric CRL4^{DCAF1} counteracts neddylation and deneddylation

In our MALS studies, the neddylated CRL4^{DCAF1} complex predominantly existed in a dimeric state (Fig 1C). To test whether the tetramer allows for direct access of the neddylation machinery, we used the tetrameric CRL4^{DCAF1} cryo-EM map and modeled the position of the putative RBX1-UBC12 complex (PDB 4P5O) (Fig 4A). The presence of UBC12, the NEDD8 E2, resulted in substantial steric clashes with the neighboring DCAF1 molecule (Fig 4A), suggesting that the tetrameric confirmation of CRL4^{DCAF1} is inhibitory to neddylation without structural rearrangements. To test this hypothesis, we established a neddylation assay, where we directly compared the amount of neddylated CRL4^{DCAF1} (WT) and CRL4^{DCAF1} (R1247A) dimeric mutant. While CRL4^{DCAF1} (R1247A) is efficiently and fully neddylated by UBC12 within 1 min (Fig 4B, left panel), the tetrameric CRL4^{DCAF1} is substantially more resistant to neddylation, as evident by longer incubation times, of up to 180 min,
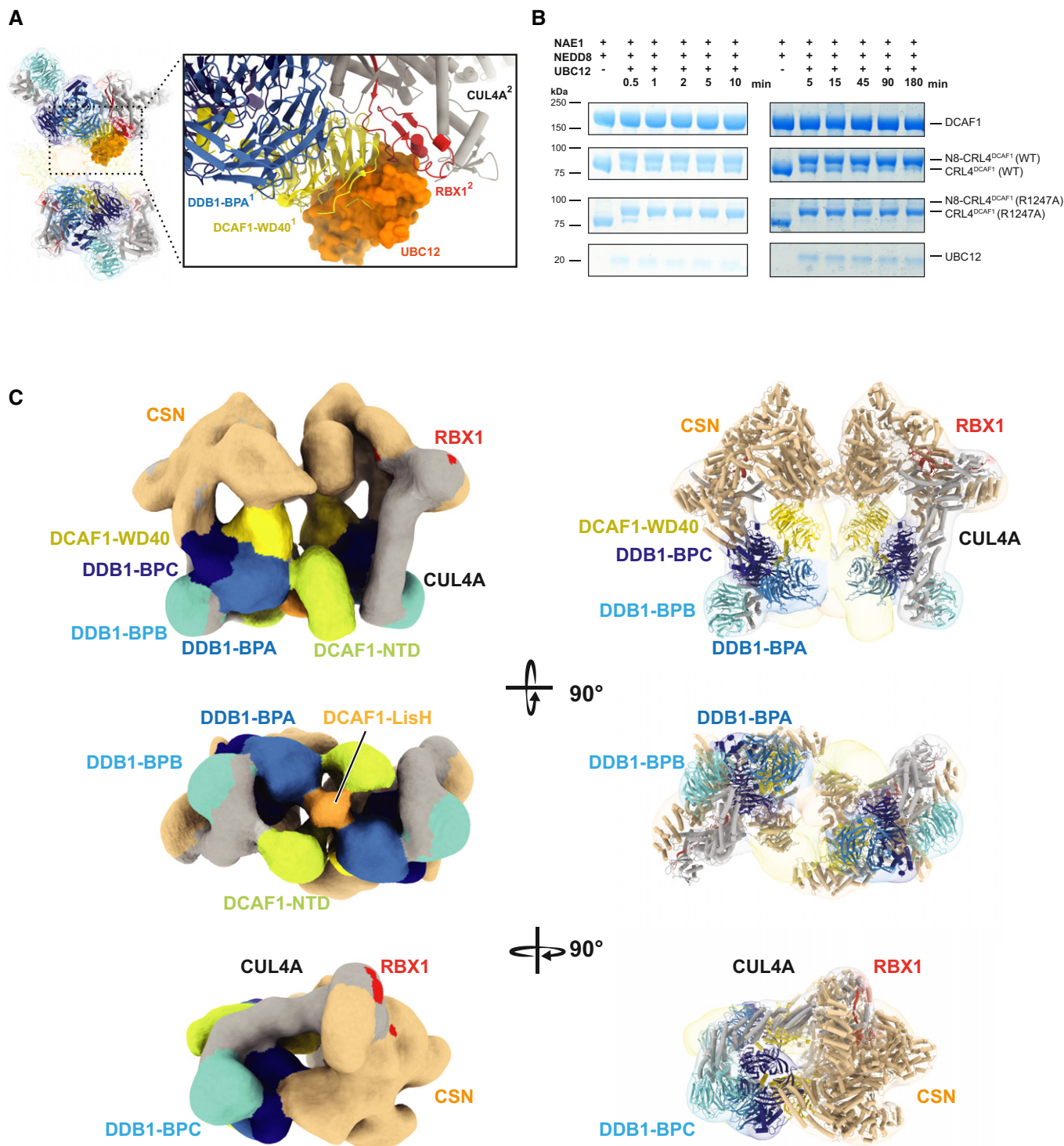
Figure 4. The tetrameric conformation renders CRL4^DCAF1 refractory toward regulation by neddylation and deneddylation.

A CRL4^DCAF1 cryo-EM map and a close-up view of fitted UBC12-RBX1 structure (PDB 4P5O) that shows steric clashes with DCAF1 (WD40)[1] of one CRL4^DCAF1 molecule (yellow) (PDB 5JK7) and RBX1[2] of the second CRL4^DCAF1 molecule (red), UBC12 is shown in orange (PDB 4P5O), DDB1 BPA (light blue), BPB (cyan), and BPC (dark blue), CUL4A in gray. Molecules belonging to different protomers are indicated by superscripts (1 or 2).

B SDS–PAGE showing the neddylation reaction time course of CRL4^DCAF1 (FL) WT and CRL4^DCAF1 (FL) (R1247A) mutant in the presence of 1 μM UBC12 for 0 to 180 min as indicated. Left panel with t = 0 to 10 min, and right panel with t = 5 to 180 min (n = 3).

C Different views of CRL4^DCAF1-CSN cryo-EM map with fitted crystal structures of CUL4A (gray) (PDB 2HYE), RBX1 (red), DDB1 BPA (light blue), BPB (cyan), BPC (dark blue), DCAF1 WD40 (yellow), DCAF1 NTD (yellow-green), and CSN (PDB 4D10) (wheat).

Source data are available online for this figure.

required to fully neddylate the CRL4^{DCAF1} (WT) complex (Fig 4B, right panel). These data illustrate the inhibitory effect of RBX1 sequestration by DCAF1 (WD40) in the tetrameric CRL4^{DCAF1} conformation. Within the dimer to tetramer equilibrium, it is the dimeric form of CRL4^{DCAF1} that likely is preferentially neddylated.

The impaired neddylation of tetrameric CRL4^{DCAF1} led us to investigate deneddylation, the opposing regulatory mechanism for CRLs catalyzed by the COP9 signalosome (CSN). Fitting the crystal structure of CSN (PDB 4D10) into the tetrameric CRL4^{DCAF1} cryo-EM map suggests that tetramerization and CSN binding are mutually exclusive. This is evident in the steric clashes between CSN and the CRL4^{DCAF1} tetramer (Fig EV4A). As previously reported, neddylated CRLs (N8-CRLs) bind CSN with very high affinity (Cavadini *et al*, 2016; Mosadeghi *et al*, 2016). The unneddylated CRLs, on the other hand, bind CSN with significantly lower affinities (Cavadini *et al*, 2016). Pull-down assays using an active site mutant of CSN (CSN5 E76A) and CRL4^{DCAF1} (FL) or a CRL4$^{DCAF1(\Delta NTD)}$ mutant, which lacks the N-terminus (973–1,507), shows that N8-CRL4^{DCAF1} (FL) and N8-CRL4$^{DCAF1(\Delta NTD)}$ form stoichiometric complexes with CSN (Fig EV4B, lanes 1 and 4). While the unneddylated CRL4$^{DCAF1(\Delta NTD)}$ shows residual binding to CSN, this ability is almost completely abolished in the case of the CRL4^{DCAF1} (FL) tetramer (Fig EV4B, lanes 2 and 3). Consistent with these findings, a 20 Å cryo-EM map of the N8-CRL4^{DCAF1}-CSN complex shows that the complex adopts a dimeric architecture when bound to CSN, revealing the central LisH-mediated elemental dimer (Figs 4C and EV4C–E). Taken together, tetramerization of CRL4^{DCAF1} is a conformational state of the ligase that interferes with CSN binding and activation.

Viral substrate binding to CRL4^{DCAF1} favors the active, dimeric state of the ligase

During its maturation cycle, HIV-1 hijacks the CRL4^{DCAF1} ligase *via* its VPR accessory protein, which binds the WD40 domain of DCAF1 and recruits host UNG2 for ubiquitination and subsequent degradation (Ahn *et al*, 2010; Wu *et al*, 2016). We set out to examine this viral-induced DCAF1 substrate for its ability to break the tetrameric CRL4^{DCAF1} complex up into dimers. We generated CRL4^{DCAF1}-VPR and CRL4^{DCAF1}-VPR-UNG2 complexes (Fig 5A), and analyzed them in SEC-MALS. The SEC-MALS analysis of CRL4^{DCAF1}-VPR-UNG2 shows that the complex exists predominantly in its dimeric form when the VPR-UNG2 substrate is bound (Fig 5B). In contrast, binding to VPR alone is compatible with the tetrameric conformation (Fig 5B). Consistent with the oligomeric states observed in SEC-MALS, fitting the crystal structure of DDB1-DCAF1(WD40)-VPR-UNG2 (PDB 5JK7) into the EM density obtained for the CRL4^{DCAF1} tetramer shows steric clashes between VPR-UNG2 and the WD40 domain of the neighboring DCAF1 molecule (Fig 5C). These data illustrate that the substrate-like UNG2 protein affects the CRL4^{DCAF1} oligomeric state similar to neddylation by favoring a dimeric CRL^{DCAF1} state. Neddylation and substrate binding thus biochemically work hand-in-hand to induce and maintain the dimeric form of CRL4^{DCAF1}, a state that represents the active form of the CRL4^{DCAF1} ligase.

We next sought to investigate the effect of a non-substrate binding protein, such as MERLIN, on the tetrameric conformation of CRL4^{DCAF1} (Fig 5D). MERLIN was shown to regulate the CRL4^{DCAF1} ligase activity (Li *et al*, 2010). We carried out SEC-MALS analysis on the CRL4^{DCAF1}-MERLIN complex. MERLIN co-migration in SEC-MALS demonstrated that MERLIN is compatible with the tetrameric assembly of CRL4^{DCAF1} (Fig 5E), which in turn suggests that MERLIN does not act like a DCAF1 substrate.

Previous studies indicate that CSN can distinguish between substrate-bound and substrate-free CRL ligases through a steric mechanism (Enchev *et al*, 2012; Cavadini *et al*, 2016), where substrate-bound CRLs clash into CSN, and are thus less effectively deneddylated than substrate-free ligases. Consistently, fitting the crystal structure of DDB1-DCAF1(WD40)-VPR-UNG2 (PDB 5Jk7) into the CRL4^{DCAF1}-CSN cryo-EM map shows significant steric clashes between VPR-UNG2 and CSN (Fig EV5D). We therefore established a fluorescence-based CSN deneddylation assay as a complementary approach to examine whether UNG2 and MERLIN function as substrates in regard to CSN regulation. Similar to other substrate-bound CRL, VPR-UNG2 binding to the N8-CRL4^{DCAF1} ligase inhibits CSN catalysis (Fig EV5E). MERLIN-bound N8-CRL4^{DCAF1}, on the other hand, is readily deneddylated by CSN, showing a comparable K_{cat} value to that of wild-type N8-CRL4^{DCAF1} (Fig EV5F). The CSN catalysis assay, along with the tetramer to dimer switch of CRL4^{DCAF1} in the presence of substrates, supports the notion that VPR-UNG2 functions analogous to a substrate protein when bound to CRL4^{DCAF1}, while MERLIN does not. This is consistent with the VPR-UNG2-DCAF1 X-ray structure (Wu *et al*, 2016), which places UNG2 in a position where it would collide with CSN in the low-resolution CSN-CRL4^{DCAF1} map (Fig EV5D) and where substrates of WD40 containing CUL4 ligases are typically bound. Substrate binding thus is incompatible with the tetrameric state of CRL4^{DCAF1}, and bound substrates instead favor the dimeric, active form of the CRL4^{DCAF1} ligase.

Discussion

We herein provide the subnanometer map of the CRL4^{DCAF1} E3 ubiquitin ligase, as well as the mechanistic characterization of this essential ubiquitin ligase. We identify a tetrameric CRL4^{DCAF1} state that counteracts neddylation (Fig 4B) and auto-ubiquitination (Fig 3C) and by these measures likely represents the inhibited state of the E3 ubiquitin ligase. Substrate binding to CRL4^{DCAF1} favors a dimeric, active conformation, which is also the preferred substrate of CSN, further underlining that this is the active conformation of the ligase. Structurally, the mechanism of DCAF1 inhibition by RBX1 sequestration is reminiscent of what has been previously observed for CSN2/RBX1 interactions in CSN structures (Emberley *et al*, 2012; Cavadini *et al*, 2016), as well as the arrangement seen in the GLOMULIN-CRL1-RBX1 complex (Duda *et al*, 2012). To our knowledge, this is the first report of a CRL with an inbuilt auto-inhibitory mechanism.

Several studies have suggested that the cullin CTD is flexible upon neddylation (Angers *et al*, 2006; Duda *et al*, 2008; Fischer *et al*, 2011; Baek *et al*, 2020; Banchenko *et al*, 2021). These conformational changes triggered upon neddylation in turn may also alter the interface between DCAF1 WD40 and RBX1. Unlike recent findings for the CUL1 systems (Baek *et al*, 2020), it is currently unclear how CUL4 ligases interact with ubiquitin loaded E2 enzymes. Given the extensive conformational rearrangements observed for CUL1 CTD, however, it is likely that a neddylated CRL4^{DCAF1} in its E2 ubiquitin bound form would further impair tetramer formation in
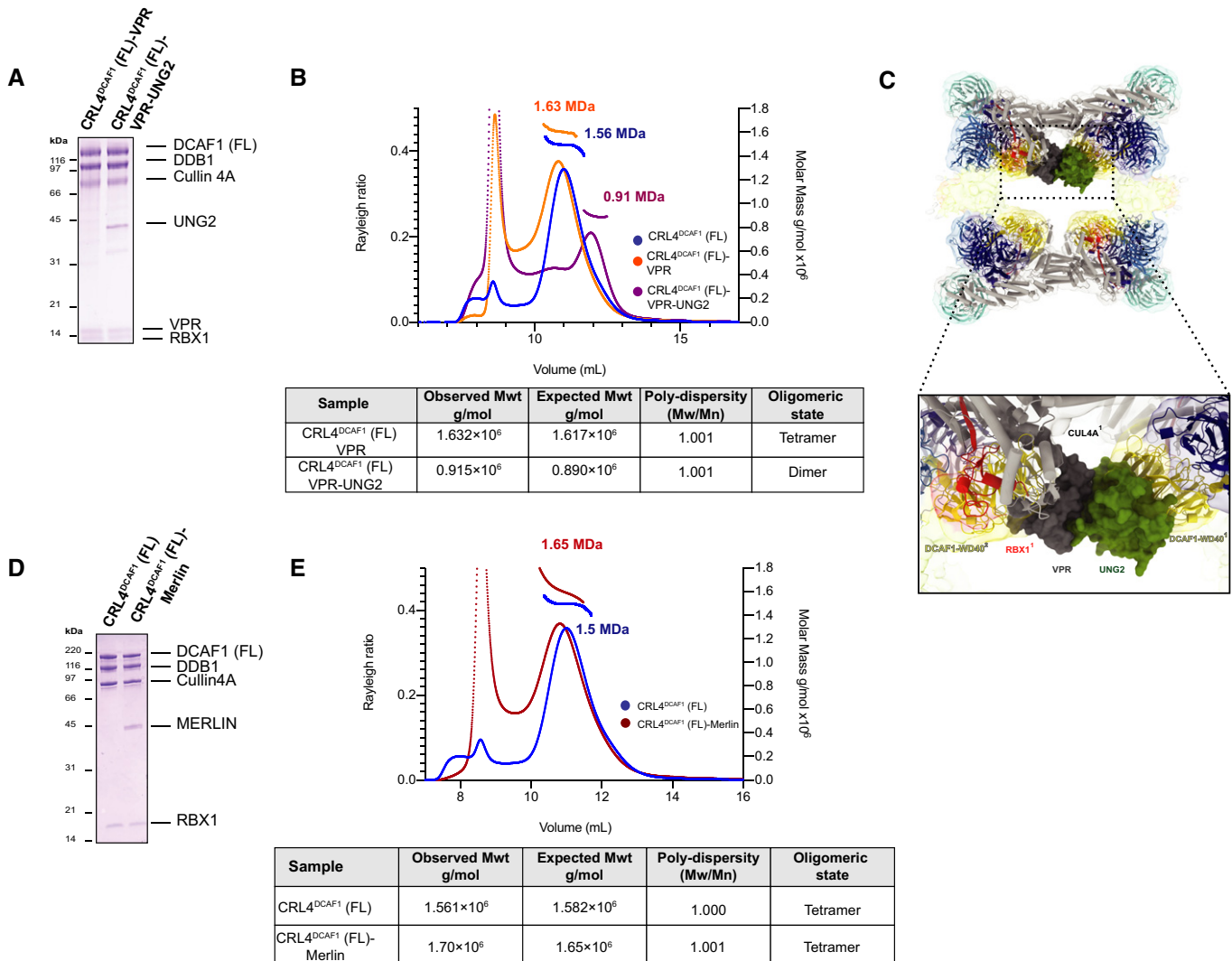
Figure 5. The effect of DCAF1 substrate versus non-substrate binding proteins on the tetrameric configuration of CRL4^{DCAF1}.

A SDS–PAGE of the purified CRL4^{DCAF1} (FL)-VPR and CRL4^{DCAF1} (FL)-VPR-UNG2 complexes.

B SEC-MALS analysis, the chromatogram shows Rayleigh ratio curves of CRL4^{DCAF1} (FL), CRL4^{DCAF1} (FL)-VPR, and CRL4^{DCAF1} (FL)-VPR-UNG2, together with the molar mass (MDa) of the main peaks determined by MALS. The table summarizes the observed molecular weight in the main peaks by SEC-MALS, listing the calculated molecular weight, polydispersity values, and oligomeric states of the tested complexes. The peaks eluting close to the void volume were shown to contain heterogeneous large aggregates (Fig EV5A and B).

C CRL4^{DCAF1} cryo-EM map with the fitted model, and a close-up view of fitted crystal structures of CUL4A (gray), RBX1 (red) (PDB 2HYE), DDB1 BPA (light blue), BPB (cyan), and BPC (dark blue), DCAF1 (WD40) (yellow), VPR (dark gray), and UNG2 (green) (PDB 5JK7).

D SDS–PAGE of the purified CRL4^{DCAF1} and CRL4^{DCAF1}(FL)-MERLIN complexes.

E SEC-MALS analysis, the chromatogram shows the Rayleigh ratio curves of CRL4^{DCAF1}(FL) (blue) and CRL4^{DCAF1}(FL)-MERLIN (red) together with the molar mass (MDa) of the main peaks calculated by MALS. The table summarizes the SEC-MALS observed molecular weights, the calculated molecular weights, polydispersity values, and oligomeric states of the tested complexes. The peak eluting close to the void volume contains large unspecific aggregates (Fig EV5C).

Source data are available online for this figure.

cells. Moreover, although our findings are consistent with CUL4^{DCAF1} being in a dimer-tetramer equilibrium, we cannot exclude that Ub/Nedd8-loaded E2 complexes, or in fact also CSN, possess additional molecular mechanisms to open the CUL4^{DCAF1} tetrameric complex and thereby convert it to a dimer.

At this stage, we can only speculate as to the enzymatic role of this inhibitory mechanism. We and others have observed spontaneous CRL4 activity and auto-ubiquitination in the absence of neddylation, in case of CRL4^{DDB2} (Scrima et al, 2008; Fischer et al, 2011; Cavadini et al, 2016), CRL4^{CRBN} (Fischer et al, 2014; Petzold et al, 2016), and CRL4^{DCAF15} (Bussiere et al, 2020) using UBCH5a as ubiquitin-conjugating enzyme. This appears to be in contrast to the CUL1 system, which has been reported to be strictly dependent on neddylation for activity (Baek et al, 2020). Furthermore, studies with CSN inhibitors have reported CRL receptor instability (Schlierf et al, 2016) due to auto-ubiquitination of the receptor following

persistent CRL activation. Although at lower flux, receptor auto-ubiquitination likely also occurs in cells with an active neddylation/deneddylation machinery. DCAF1 tetramerization may thus provide an additional layer of inhibition preventing futile DCAF1 receptor auto-ubiquitination and degradation cycles for substrate- or neddylation-free CRL4^{DCAF1}. Given the sensitivity of cells toward DCAF1 loss, this may preserve the cellular CRL4^{DCAF1} pool. A somewhat different albeit non-mutually exclusive explanation is that the inactive form of CRL4^{DCAF1} serves to counteract spurious activation of the enzymes. This would assure that only a tightly bound substrate shifts the equilibrium to a dimeric, active form of the enzyme to then bestow CRL4^{DCAF1} neddylation and full activity.

We speculate that the CRL4^{DCAF1} dimer–tetramer transition is primarily regulated through neddylation and substrate binding. However, a possible regulatory mechanism involving post-translational modifications including phosphorylation can not be excluded at this point. We note that there are a number of residues in the CUL4 C-terminus expected to be phosphorylated (S642, Y744, and N751), based on the PhosphoSitePlus resource (Hornbeck *et al*, 2015). When phosphorylated, these residues have the potential to impact tetramerization in light of our structures and would allow activation.

The pronounced pan-lethality of DCAF1 loss, suggests an important role of DCAF1 for cell survival. As CUL1-based CRLs may intrinsically be more tightly regulated by neddylation than the CRL4 family, an additional auto-inhibitory circuitry, as observed for CRL4^{DCAF1} may thus be required for proper ligase function, targeting and regulation. Future experiments are required to assess the biological role of this inhibitory mechanism, and to examine whether other oligomeric CRLs use a similar mechanism.

Materials and Methods

Cloning, protein expression, and purification

Wild-type (WT) and mutant constructs of full-length human DCAF1 (Q9Y4B6) were cloned into pLAF vector, which is derived from the pBacPAK8 system (ClonTech). Cullin 4A (FL) (Q13619) and DDB1 (FL) (Q16531) were assembled into one vector (pBIG1a) using Gibson-based technique (biGBac) (Weissmann *et al*, 2016). Recombinant baculoviruses were prepared in *Spodoptera frugiperda* (*sf9*) cells using the Bac-to-Bac system (Life Technologies). Recombinant protein complexes were expressed in *Trichoplusia ni* High Five cells by co-infection of 35 ml of single baculoviruses per 2 l of High Five culture. DCAF1 wild-type and mutants were expressed with N-terminal Strep (II) tag, and Cullin 4A and DDB1 were expressed with N-terminal His$_6$ tags. MERLIN Δ (1–346) was expressed with an N-terminal glutathione S-transferase (GST) tag. CRL4^{DCAF1}-CSN complex was co-expressed using the CSN4-RBX1 fusion construct, as described in Cavadini *et al* (2016).

Cells were harvested 36–48 h after infection and lysed by sonication in 50 mM tris(hydroxymethyl)aminomethane hydrochloride (Tris-HCl) pH 8.0, 200 mM NaCl, 0.5 mM tris(2-carboxyethyl) phosphine (TCEP), including 0.1% Triton X-100, 1x protease inhibitor cocktail (Roche Applied Science), and 1 mM phenylmethanesulfonyl fluoride (PMSF). This was followed by ultracentrifugation at 40,000 *g* for 45 min to separate the soluble fraction of the lysate (supernatant). The supernatant was loaded on Strep-Tactin (IBA life

sciences) affinity chromatography in buffer containing 50 mM Tris-HCl pH 7.5, 200 mM NaCl, 0.5 mM TCEP. The Strep (II) elution fractions were further purified via ion exchange chromatography (Poros HQ 50 μm, Life Technologies) and subjected to size-exclusion chromatography (Superose 6, GE Healthcare) in a buffer containing 50 mM HEPES pH 7.4, 200 mM NaCl, and 0.25 mM TCEP. Pure fractions were collected and concentrated using 10,000 MWT cut-off centrifugal devices (PALL) and stored at −80°C.

APPBP1-UBA3, UBC12, and NEDD8 were expressed and purified as described before Duda *et al* (2008), Huang *et al* (2007), and Huang *et al* (2008).

In vitro Ubiquitination of CRL4^{DCAF1}

In vitro ubiquitination was performed by mixing wild-type or mutant CRL4^{DCAF1} at 2 μM with a reaction mixture containing E1 (UBA1, Boston Biochem) at 0.1 μM, E2 (UBCH5a, Boston Biochem) at 0.1 μM, wild-type Ubiquitin (Ubiquitin, Boston Biochem) at 5 μM as indicated. Reactions were carried out in 50 mM Tris pH 7.7, 200 mM NaCl, 10 mM MgCl$_2$, 0.2 mM CaCl$_2$, 3 mM ATP, 2 mM DTT, and 0.1 mg/ml BSA, and incubated for 0–15 min at 30°C. Reactions were then analyzed by Western blot using anti-ubiquitin (P4D1) primary antibody (Santa Cruz, 1:500) and Horseradish Peroxidase (HRP) conjugated anti-rabbit secondary antibody (1:10,000). Blots were incubated with SuperSignal™ West Pico PLUS Chemiluminescent Substrate solution (Thermo Fisher) and scanned on Fusion FX7 imaging system (Witec AG).

Pull-down assay of CRL4^{DCAF1} and CSN

N8-CRL4^{DCAF1} (FL), N8-CRL4$^{DCAF1(ΔNTD)}$ (987–1,507), CRL4^{DCAF1} (FL), and CRL4$^{DCAF1(ΔNTD)}$ were loaded on 20 μl Strep-Tactin Macroprep beads (IBA life sciences), and incubated with untagged and inactive CSN (CSN5 E76A) at 1:1 molar ratio for 1 h at 4°C. Bound complexes were washed three times with 1 ml buffer containing 50 mM HEPES pH 7.4, 200 mM NaCl, and 0.25 mM TCEP. Beads were boiled in SDS loading dye.

Size-Exclusion Chromatography-Multi-Angle Light Scattering (SEC-MALS)

The molecular masses of CRL4^{DCAF1} WT and mutant complexes were investigated by SEC-MALS using an ÄKTA FPLC system (GE Healthcare) equipped with a Superose 6 10/300 size-exclusion column (GE Healthcare Life Sciences). 50 μl of the protein samples at a concentration of 2 mg/ml was loaded. The light scattering measurements in the SEC-MALS system used an Optilab T-rEX refractive index detector and a miniDAWN TREOS 3 angle MALS detector (Wyatt Technology). The samples were loaded on the SEC-MALS system in a buffer containing 50 mM HEPES pH 7.4, 200 mM NaCl and 1 mM TCEP. The protein fractions at/near the void volume eluted as heterogeneous high molecular weight aggregates, and we therefore did not further investigate their behavior (Fig EV5A–C).

Cryo-electron microscopy and image processing

In order to increase the stability of the CRL4^{DCAF1} and CRL4^{DCAF1}-CSN complexes, gradient fixation (GraFix) protocol was performed

(Stark, 2010). The samples were loaded on a glycerol gradient (10–30% w/v) in the presence of the cross-linker glutaraldehyde (0.25% v/v) followed by ultracentrifugation (SW40Ti rotor) at 30,000 rpm for 19 h at 4°C. Peak fractions containing CRL4^{DCAF1}, or CRL4^{DCAF1}-CSN complexes were collected and concentrated. For CRL4^{DCAF1}-CSN, glycerol removal and buffer exchange was performed by several rounds of concentration and dilution using 10,000 MWT cutoff centrifugal devices (PALL). Glycerol removal from the CRL4^{DCAF1} sample was performed by injecting the sample into Superose 6 3.2/300 in buffer containing 50 mM HEPES pH7.4, 200 mM NaCl, and 1 mM TCEP, and collecting the peak fraction. 4 μl sample (0.1–0.2 mg/ml) was applied on glow discharged Quantifoil holey carbon grids. For the CRL4^{DCAF1} samples, R1.2/1.3, Cu 400 mesh grids were used for data collection (Quantifoil Micro Tools GmbH, Grosslöbichau, Germany). For the CRL4^{DCAF1}-CSN sample, Lacey carbon grids (Ted Pella, Inc.) were used. For both samples, CRL4^{DCAF1} and CRL4^{DCAF1}-CSN, grids were manually floated with continuous carbon films. Grids were incubated for 30 s at 4°C and 100% humidity, and immediately blotted with Whatman no. 1 filter paper (blotting time 2 s) and vitrified by plunging into liquid ethane (Leica EM GP plunger).

For CRL4^{DCAF1}, micrographs were recorded on a Cs corrected FEI Titan Krios TEM (Thermo Fisher) operated at 300 kV, using a Gatan K2-summit direct electron detector after a Quantum-LS energy filter with a slit width of 30 eV (Gatan) (Table EV1). The micrographs were recorded in electron-counting mode with a dose rate of 5 e$^-$/pixel/s. The raw stacks were recorded with 40 frames and an exposure time of 9 s, yielding a total dose of 45 e$^-$/pixel. Micrographs were recorded with a magnification of ×130,000 resulting in a calibrated pixel size of 0.88 Å. Defocus values varied between −1.5 and −4 μm.

1,280 micrographs were processed. Dose-fractionated raw stacks were subjected to drift correction using Unblur (Campbell et al, 2012). The contrast transfer function (CTF) was estimated using CTFFIND4 (Rohou & Grigorieff, 2015). Particles were selected by Gautomatch (developed by Kai Zhang, http://www.mrc-lmb.cam.ac.uk/kzhang/Gautomatch/). 158,188 Particles were imported into RELION and extracted with a box size of 260 × 260 pixels after binning the micrographs by a factor of 2 (1.76 Å/pixel). After four rounds of 2D classification, a subset of particles were used to generate an ab initio model in SPARX (Penczek et al, 1994; Baldwin & Penczek, 2007; Hohn et al, 2007). Two rounds of 3D classification were performed to remove heterogeneous particles (Fig EV2). 3D refinement on 14,000 particles after applying D2 symmetry yielded the final map at 8.4 Å. Post-processing was done using a mask created in RELION by extending the binary map with three pixels and adding three pixels of soft edge. The binarization threshold was set to 0.0096.

For CRL4^{DCAF1}-CSN complex, micrographs were recorded on a FEI F30 Polara (Thermo Fisher) operated at 300 kV, using a Gatan K2-summit direct electron detector in electron-counting mode (magnification of x31,000 and calibrated pixel size of 1.24 Å). The micrographs were exposed for 16 s and dose fractionated into 40 frames. Defocus values varied between −1.5 and −4 μm. 1,185 micrographs were processed. Dose-fractionated raw stacks were subjected to drift correction using unblur (Campbell et al, 2012). CTF was estimated using CTFFIND (Rohou & Grigorieff, 2015). Particles were auto-picked in RELION 1.4. 173,061 particles were

extracted after binning the micrographs by a factor of 2 (2.48 Å/pixel). Two rounds of 2D classification and one round of 3D classification were performed to remove heterogeneous particles. 3D refinement on 26,582 particles after applying C2 symmetry yielded the final map at 23 Å.

Model building and refinement

The two template structures with PDB IDs 2HYE and 5JK7 were iteratively re-refined against the crystallographic structure factors using Coot and Phenix (Angers et al, 2006; Emsley et al, 2010; Wu et al, 2016; Liebschner et al, 2019). The template models for CUL4A, RBX1, and DDB1 BPB were extracted from coordinates with PDB ID 2HYE (Table EV2), and the template models for DCAF1 and DDB1 BPA/BPC were extracted from coordinates with PDB ID 5JK7 and docked into the cryo-EM map using Chimera (Pettersen et al, 2004). The structure was then refined using the Rosetta density-guided FastRelax protocol (torsional followed by Cartesian space) in combination with constraints to the starting model coordinates and symmetric scoring (Wang et al, 2016b). Before deposition, the model was truncated to poly-alanine and validation was performed using Phenix and Molprobity (Chen et al, 2009). Figures were generated using ChimeraX (Pettersen et al, 2020).

Modeling of DCAF1 N-terminal domains

The DCAF1 LisH domain (aa 846–883) was predicted using the Rosetta comparative modeling protocol provided through the Robetta server (Raman et al, 2009; Song et al, 2013). The top-ranked model was used for superposition on a homologous LisH homodimer (PDB 6IWV, (Wang et al, 2019)), and the resulting dimer was docked into the density using Chimera (Pettersen et al, 2004). The homodimer homology model was validated by docking simulations using the Rosetta symmetric docking protocol (5,000 decoys, André et al, 2007).

The DCAF1 Armadillo domain (aa 1–845) was predicted using Alphafold v2.0 (Jumper et al, 2021). The portion between aa 507 and 817 was extracted and insertions between ARM repeats were removed. The resulting model was rigid body-docked into the density using Chimera and Coot and the density fit of the α-helical bundles was evaluated by calculating the correlation between a simulated model-map (8.4 Å) and the experimental map using the Chimera.

Labeling of NEDD8 with PET22-maleimide

The purified human NEDD8 mutant (Methionine 1 to Cysteine, M1C) was incubated with 8 mM DTT at 4°C for 1 h to completely reduce the protein sample. Buffer exchange was performed in non-reducing buffer conditions, 50 mM Tris pH 7.5 and 150 mM NaCl. PT22-maleimide (TTP Labtech) were dissolved in 100% DMSO and mixed with NEDD8 in 4:1 ratio. The labeling reaction took place at room temperature after 3-h incubation in a vacuum desiccator, and the reaction continued overnight at 4°C. Labeled NEDD8 was purified on a Superdex 200 16/60 column in 50 mM Tris pH 7.5, 150 mM NaCl, 0.25 mM TCEP, and 10% (v/v) glycerol. The sample was then concentrated and stored at −80°C.

Neddylation of Cullin 4 with wild-type or fluorophore-labeled NEDD8

In vitro neddylation was performed by mixing wild-type or mutant CRL4^{DCAF1} at 2 μM with a reaction mixture containing 0.15 μM APPBP1-UBA3, 6 μM wild-type NEDD8, and 1 μM UBC12. Reactions were carried out in 50 mM Tris-HCl pH 7.7, 200 mM NaCl, 2.5 mM MgCl$_2$, 5 mM DTT, and 1.25 mM ATP, and incubated at room temperature for 5–180 min as indicated.

The neddylation reaction with the fluorophore-labeled NEDD8 involves 0.3 μM APPBP1-UBA3, 1.2 μM UBC12, 4–8 μM CRL4^{DCAF1}, 8–20 μM NEDD8, 2.5 mM MgCl$_2$, and 1.25 mM ATP. The reaction was carried out in HEPES pH7.4, 200 mM NaCl, and 1 mM TCEP buffer at room temperature.

Fluorescence polarization (FP)-based CSN activity assays

NEDD8 was labeled with PT22-maleimide (TTP Labtech) and enzymatically conjugated to CRLs as described. 7- to 10-μl reaction mix contains 50 mM Tris-HCl pH7.5, 200 mM NaCl, and 1 mM TCEP, 0.1% pluronic acid, and different concentrations of PT22-labeled CRL4^{DCAF1} (80 nM–1.5μM), and 15 nM CSN wild-type for CRL4^{DCAF1} and CRL4^{DCAF1}- MERLIN (1–346), and 150 nM CSN wild-type for CRL4^{DCAF1}-VPR and CRL4^{DCAF1}-VPR-UNG2. Reactions took place at room temperature in 384-well plates in a BMG PheraStar plate reader (BMG LabTech). Initial rates were calculated by measuring the change in fluorescence polarization at 590 nm after excitation at 540 nm. Product formation was calculated as described in (Marks *et al*, 2005). Initial rate constants were calculated by plotting product formation (M) over time (s) using GraphPad Prism version 7.00 (GraphPad Software). K_m and K_{cat} were calculated by non-linear fitting of initial velocities V_0 in the Michaelis–Menten equation.

Data availability

The cryo-EM maps of the CRL4^{DCAF1} and CRL4^{DCAF1}-CSN complexes are deposited in the Electron Microscopy databank under the accession codes EMD-12964 (https://www.ebi.ac.uk/emdb/entry/EMD-12964) and EMD-12965 (https://www.ebi.ac.uk/emdb/entry/EMD-12965), respectively. The model coordinates for the CRL4^{DCAF1} structure are deposited in the Protein Data Bank under the accession code 7OKQ (https://www.rcsb.org/structure/7OKQ). Table EV1 summaries cryo-EM data collection, refinement, and validation statistics. Table EV2 includes the validation statistics for re-refined template models.

Expanded View for this article is available online.

Conflict of interest

The authors declare that they have no conflict of interest.

References

Ahn J, Vu T, Novince Z, Guerrero-Santoro J, Rapic-Otrin V, Gronenborn AM (2010) HIV-1 Vpr loads uracil DNA glycosylase-2 onto DCAF1, a substrate recognition subunit of a cullin 4A-ring E3 ubiquitin ligase for proteasome-dependent degradation. *J Biol Chem* 285: 37333–37341

Ahn J, Novince Z, Concel J, Byeon C-H, Makhov AM, Byeon I-JL, Zhang P, Gronenborn AM (2011) The Cullin-RING E3 ubiquitin ligase CRL4–DCAF1 complex dimerizes via a short helical region in DCAF1. *Biochemistry* 50: 1359–1367

André I, Bradley P, Wang C, Baker D (2007) Prediction of the structure of symmetrical protein assemblies. *Proc Natl Acad Sci USA* 104: 17656–17661

Angers S, Li T, Yi X, MacCoss MJ, Moon RT, Zheng N (2006) Molecular architecture and assembly of the DDB1-CUL4A ubiquitin ligase machinery. *Nature* 443: 590–593

Baek K, Krist DT, Prabu JR, Hill S, Klügel M, Neumaier L-M, Gronau S, Kleiger G, Schulman BA (2020) NEDD8 nucleates a multivalent cullin–RING–UBE2D ubiquitin ligation assembly. *Nature* 578: 461–466

Baldauf H-M, Stegmann L, Schwarz S-M, Ambiel I, Trotard M, Martin M, Burggraf M, Lenzi GM, Lejk H, Pan X *et al* (2017) Vpx overcomes a SAMHD1-independent block to HIV reverse transcription that is specific to resting CD4 T cells. *Proc Natl Acad Sci USA* 114: 2729–2734

Baldwin PR, Penczek PA (2007) The transform class in SPARX and EMAN2. *J Struct Biol* 157: 250–261

Banchenko S, Krupp F, Gotthold C, Bürger J, Graziadei A, O'Reilly FJ, Sinn L, Ruda O, Rappsilber J, Spahn CMT *et al* (2021) Structural insights into Cullin4-RING ubiquitin ligase remodelling by Vpr from simian immunodeficiency viruses. *Plos Pathog* 17: e1009775

Bussiere DE, Xie L, Srinivas H, Shu W, Burke A, Be C, Zhao J, Godbole A, King D, Karki RG *et al* (2020) Structural basis of indisulam-mediated RBM39 recruitment to DCAF15 E3 ligase complex. *Nat Chem Biol* 16: 15–23

Campbell M, Cheng A, Brilot A, Moeller A, Lyumkis D, Veesler D, Pan J, Harrison S, Potter C, Carragher B *et al* (2012) Movies of ice-embedded particles enhance resolution in electron cryo-microscopy. *Structure* 20: 1823–1828

Cavadini S, Fischer ES, Bunker RD, Potenza A, Lingaraju GM, Goldie KN, Mohamed WI, Faty M, Petzold G, Beckwith REJ *et al* (2016) Cullin–RING ubiquitin E3 ligase regulation by the COP9 signalosome. *Nature* 531: 598–603

Chen VB, Arendall III WB, Headd JJ, Keedy DA, Immormino RM, Kapral GJ, Murray LW, Richardson JS, Richardson DC (2009) MolProbity: all-atom structure validation for macromolecular crystallography. *Acta Crystallogr D Biol Crystallogr* 66: 12–21

Duda DM, Borg LA, Scott DC, Hunt HW, Hammel M, Schulman BA (2008) Structural insights into NEDD8 activation of cullin-RING ligases: conformational control of conjugation. *Cell* 134: 995–1006

Duda DM, Olszewski JL, Tron AE, Hammel M, Lambert LJ, Waddell MB, Mittag T, DeCaprio JA, Schulman BA (2012) Structure of a glomulin-RBX1-CUL1 complex: inhibition of a RING E3 ligase through masking of its E2-binding surface. *Mol Cell* 47: 371–382

Emberley ED, Mosadeghi R, Deshaies RJ (2012) Deconjugation of Nedd8 from Cul1 is directly regulated by Skp1-F-box and substrate, and the COP9 signalosome inhibits deneddylated SCF by a noncatalytic mechanism. *J Biol Chem* 287: 29679–29689

Emsley P, Lohkamp B, Scott WG, Cowtan K (2010) Features and development of Coot. *Acta Cryst* D66: 486–501

Enchev RI, Scott DC, da Fonseca PCA, Schreiber A, Monda JK, Schulman BA, Peter M, Morris EP (2012) Structural basis for a reciprocal regulation between SCF and CSN. *Cell Rep* 2: 616–627

Fischer ES, Scrima A, Böhm K, Matsumoto S, Lingaraju GM, Faty M, Yasuda T, Cavadini S, Wakasugi M, Hanaoka F *et al* (2011) The molecular basis of CRL4. *Cell* 147: 1024–1039

Fischer ES, Böhm K, Lydeard JR, Yang H, Stadler MB, Cavadini S, Nagel J, Serluca F, Acker V, Lingaraju GM *et al* (2014) Structure of the DDB1-CRBN E3 ubiquitin ligase in complex with thalidomide. *Nature* 512: 49–53

Guo Z, Kong Q, Liu C, Zhang S, Zou L, Yan F, Whitmire JK, Xiong Y, Chen X, Wan YY (2016) DCAF1 controls T-cell function via p53-dependent and -independent mechanisms. *Nat Commun* 7: 1–13

Heusel M, Bludau I, Rosenberger G, Hafen R, Frank M, Banaei Esfahani A, Drogen A, Collins BC, Gstaiger M, Aebersold R (2019) Complex-centric proteome profiling by SEC- SWATH- MS. *Mol Syst Biol* 15: 24–22

Hohn M, Tang G, Goodyear G, Baldwin PR, Huang Z, Penczek PA, Yang C, Glaeser RM, Adams PD, Ludtke SJ (2007) SPARX, a new environment for Cryo-EM image processing. *J Struct Biol* 157: 47–55

Hornbeck PV, Zhang B, Murray B, Kornhauser JM, Latham V, Skrzypek E (2015) PhosphoSitePlus, 2014: mutations, PTMs and recalibrations. *Nucleic Acids Res* 43: D512–D520

Hrecka K, Gierszewska M, Srivastava S, Kozaczkiewicz L, Swanson SK, Florens L, Washburn MP, Skowronski J (2007) Lentiviral Vpr usurps Cul4–DDB1 [VprBP] E3 ubiquitin ligase to modulate cell cycle. *Proc Natl Acad Sci USA* 104: 11778–11783

Huang DT, Hunt HW, Zhuang M, Ohi MD, Holton JM, Schulman BA (2007) Basis for a ubiquitin-like protein thioester switch toggling E1–E2 affinity. *Nature* 445: 394–398

Huang DT, Zhuang M, Ayrault O, Schulman BA (2008) Identification of conjugation specificity determinants unmasks vestigial preference for ubiquitin within the NEDD8 E2. *Nat Struct Mol Biol* 15: 280–287

Jumper J, Evans R, Pritzel A, Green T, Figurnov M, Ronneberger O, Tunyasuvunakool K, Bates R, Žídek A, Potapenko A *et al* (2021) Highly accurate protein structure prediction with AlphaFold. *Nature* 596: 583–589

Kaur M, Khan MM, Kar A, Sharma A, Saxena S (2012) CRL4-DDB1-VPRBP ubiquitin ligase mediates the stress triggered proteolysis of Mcm10. *Nucleic Acids Res* 40: 7332–7346

Kim MH, Cooper DR, Oleksy A, Devedjiev Y, Derewenda U, Reiner O, Otlewski J, Derewenda ZS (2004) The structure of the N-terminal domain of the product of the lissencephaly gene Lis1 and its functional implications. *Structure* 12: 987–998

Kim K, Heo K, Choi J, Jackson S, Kim H, Xiong Y, An W (2012) Vpr-binding protein antagonizes p53-mediated transcription via direct interaction with H3 tail. *Mol Cell Biol* 32: 783–796

Kim K, Kim J-M, Kim J-S, Choi J, Lee YS, Neamati N, Song JS, Heo K, An W (2013) VprBP has intrinsic kinase activity targeting histone H2A and represses gene transcription. *Mol Cell* 52: 459–467

König R, Chiang C-Y, Tu BP, Yan SF, DeJesus PD, Romero A, Bergauer T, Orth A, Krueger U, Zhou Y *et al* (2007) A probability-based approach for the analysis of large-scale RNAi screens. *Nat Methods* 4: 847–849

Kyei GB, Cheng X, Ramani R, Ratner L (2015) Cyclin L2 is a critical HIV dependency factor in macrophages that controls SAMHD1 abundance. *Cell Host Microbe* 17: 98–106

Li W, You L, Cooper J, Schiavon G, Pepe-Caprio A, Zhou L, Ishii R, Giovannini M, Hanemann CO, Long SB *et al* (2010) Merlin/NF2 suppresses tumorigenesis by inhibiting the E3 ubiquitin ligase CRL4DCAF1 in the nucleus. *Cell* 140: 477–490

Li W, Cooper J, Zhou L, Yang C, Erdjument-Bromage H, Zagzag D, Snuderl M, Ladanyi M, Hanemann CO, Zhou P *et al* (2014) Merlin/NF2 loss-driven tumorigenesis linked to CRL4. *Cancer Cell* 26: 48–60

Liebschner D, Afonine PV, Baker ML, Bunkoczi G, Chen VB, Croll TI, Hintze B, Hung LW, Jain S, McCoy AJ *et al* (2019) Macromolecular structure determination using X-rays, neutrons and electrons: recent developments in Phenix. *Acta Cryst* D75: 861–877

Lingaraju GM, Bunker RD, Cavadini S, Hess D, Hassiepen U, Renatus M, Fischer ES, Thomä NH (2014) Crystal structure of the human COP9 signalosome. *Nature* 512: 161–165

Marks BD, Qadir N, Eliason HC, Shekhani MS, Doering K, Vogel KW (2005) Multiparameter analysis of a screen for progesterone receptor ligands: comparing fluorescence lifetime and fluorescence polarization measurements. *Assay Drug Dev Techn* 3: 613–622

McCall CM, Miliani de Marval PL, Chastain PD, Jackson SC, He YJ, Kotake Y, Cook JG, Xiong Y (2008) Human immunodeficiency virus type 1 Vpr-binding protein VprBP, a WD40 protein associated with the DDB1-CUL4 E3 ubiquitin ligase, is essential for DNA replication and embryonic development. *Mol Cell Biol* 28: 5621–5633

McDonald ER, de Weck A, Schlabach MR, Billy E, Mavrakis KJ, Hoffman GR, Belur D, Castelletti D, Frias E, Gampa K *et al* (2017) Project DRIVE: a compendium of cancer dependencies and synthetic lethal relationships uncovered by large-scale, deep RNAi screening. *Cell* 170: 577–592

Mori T, Gotoh S, Shirakawa M, Hakoshima T (2014) Structural basis of DDB1-and-Cullin 4-associated Factor 1 (DCAF1) recognition by merlin/NF2 and its implication in tumorigenesis by CD44-mediated inhibition of merlin suppression of DCAF1 function. *Genes Cells* 19: 603–619

Mosadeghi R, Reichermeier KM, Winkler M, Schreiber A, Reitsma JM, Zhang Y, Stengel F, Cao J, Kim M, Sweredoski MJ *et al* (2016) Structural and kinetic analysis of the COP9-Signalosome activation and the cullin-RING ubiquitin ligase deneddylation cycle. *eLife* 5: e12102

Penczek PA, Grassucci RA, Frank J (1994) The ribosome at improved resolution: New techniques for merging and orientation refinement in 3D cryo-electron microscopy of biological particles. *Ultramicroscopy* 53: 251–270

Pettersen EF, Goddard TD, Huang CC, Couch GS, Greenblatt DM, Meng EC, Ferrin TE (2004) UCSF Chimera–A visualization system for exploratory research and analysis. *J Comput Chem* 25: 1605–1612

Pettersen EF, Goddard TD, Huang CC, Meng EC, Couch GS, Croll TI, Morris JH, Ferrin TE (2020) UCSF ChimeraX: Structure visualization for researchers, educators, and developers. *Protein Sci* 30: 70–82

Petzold G, Fischer ES, Thomä NH (2016) Structural basis of lenalidomide-induced CK1α degradation by the CRL4CRBN ubiquitin ligase. *Nature* 532: 127–130

Pierce NW, Lee JE, Liu X, Sweredoski MJ, Graham RLJ, Larimore EA, Rome M, Zheng N, Clurman BE, Hess S *et al* (2013) Cand1 promotes assembly of new SCF complexes through dynamic exchange of F box proteins. *Cell* 153: 206–215

Raman S, Vernon R, Thompson J, Tyka M, Sadreyev R, Pei J, Kim D, Kellogg E, DiMaio F, Lange O *et al* (2009) Structure prediction for CASP8 with all-atom refinement using Rosetta. *Proteins* 77: 89–99

Reichermeier KM, Straube R, Reitsma JM, Sweredoski MJ, Rose CM, Moradian A, den Besten W, Hinkle T, Verschueren E, Petzold G *et al* (2020) PIKES analysis reveals response to degraders and key regulatory mechanisms of the CRL4 network. *Mol Cell* 77: 1092–1106

Rohou A, Grigorieff N (2015) CTFFIND4: Fast and accurate defocus estimation from electron micrographs. *J Struct Biol* 192: 216–221

Romani B, Cohen ÉA (2012) Lentivirus Vpr and Vpx accessory proteins usurp the cullin4–DDB1 (DCAF1) E3 ubiquitin ligase. *Curr Opin Virol* 2: 755–763

Schabla NM, Mondal K, Swanson PC (2019) DCAF1 (VprBP): emerging physiological roles for a unique dual-service E3 ubiquitin ligase substrate receptor. *J Mol Cell Biol* 11: 725–735

Schlierf A, Altmann E, Quancard J, Jefferson AB, Assenberg R, Renatus M, Jones M, Hassiepen U, Schaefer M, Kiffe M *et al* (2016) Targeted inhibition of the COP9 signalosome for treatment of cancer. *Nat Commun* 7: 13166

Schwefel D, Groom HCT, Boucherit VC, Christodoulou E, Walker PA, Stoye JP, Bishop KN, Taylor IA (2014) Structural basis of lentiviral subversion of a cellular protein degradation pathway. *Nature* 505: 234–238

Scrima A, Koníčková R, Czyzewski BK, Kawasaki Y, Jeffrey PD, Groisman R, Nakatani Y, Iwai S, Pavletich NP, Thomä NH (2008) Structural basis of UV DNA-damage recognition by the DDB1-DDB2 complex. *Cell* 135: 1213–1223

Shao DD, Tsherniak A, Gopal S, Weir BA, Tamayo P, Stransky N, Schumacher SE, Zack TI, Beroukhim R, Garraway LA *et al* (2013) ATARiS: Computational quantification of gene suppression phenotypes from multisample RNAi screens. *Genome Res* 23: 665–678

Song Y, DiMaio F, Wang RY-R, Kim D, Miles C, Brunette TJ, Thompson J, Baker D (2013) High-resolution comparative modeling with RosettaCM. *Structure* 21: 1735–1742

Stark H (2010) Chapter Five GraFix: stabilization of fragile macromolecular complexes for single particle cryo-EM. *Methods Enzymol* 481: 109–126

Tarricone C, Perrina F, Monzani S, Massimiliano L, Kim M-H, Derewenda ZS, Knapp S, Tsai L-H, Musacchio A (2004) Coupling PAF signaling to dynein regulation structure of LIS1 in complex with PAF-acetylhydrolase. *Neuron* 44: 809–821

Wang D, Kon N, Lasso G, Jiang LE, Leng W, Zhu W-G, Qin J, Honig B, Gu W (2016a) Acetylation-regulated interaction between p53 and SET reveals a widespread regulatory mode. *Nature* 538: 118–122

Wang RY-R, Song Y, Barad BA, Cheng Y, Fraser JS, DiMaio F (2016b) Automated structure refinement of macromolecular assemblies from cryo-EM maps using Rosetta. *eLife* 5: e17219

Wang X, Arceci A, Bird K, Mills CA, Choudhury R, Kernan JL, Zhou C, Bae-Jump V, Bowers A, Emanuele MJ (2017) VprBP/DCAF1 regulates the degradation and nonproteolytic activation of the cell cycle transcription factor FoxM1. *Mol Cell Biol* 37: e00609-16

Wang H, Wang Z, Tang Q, Yan XX, Xu W (2019) Crystal structure of the LUFS domain of human single-stranded DNA binding Protein 2 (SSBP2). *Protein Sci* 28: 788–793

Weissmann F, Petzold G, VanderLinden R, Huis in 't Veld PJ, Brown NG, Lampert F, Westermann S, Stark H, Schulman BA, Peters J-M (2016) biGBac enables rapid gene assembly for the expression of large multisubunit protein complexes. *Proc Natl Acad Sci USA* 113: E2564–E2569

Wu Y, Zhou X, Barnes CO, DeLucia M, Cohen AE, Gronenborn AM, Ahn J, Calero G (2016) The DDB1–DCAF1–Vpr–UNG2 crystal structure reveals how HIV-1 Vpr steers human UNG2 toward destruction. *Nat Struct Mol Biol* 23: 933–940

Yu C, Zhang Y-L, Pan W-W, Li X-M, Wang Z-W, Ge Z-J, Zhou J-J, Cang Y, Tong C, Sun Q-Y *et al* (2013) CRL4 complex regulates mammalian oocyte survival and reprogramming by activation of TET proteins. *Science* 342: 1518–1521

Yu C, Ji S-Y, Sha Q-Q, Sun Q-Y, Fan H-Y (2015) CRL4–DCAF1 ubiquitin E3 ligase directs protein phosphatase 2A degradation to control oocyte meiotic maturation. *Nat Commun* 6: 8017

Zhang S, Feng Y, Narayan O, Zhao L-J (2001) Cytoplasmic retention of HIV-1 regulatory protein Vpr by protein-protein interaction with a novel human cytoplasmic protein VprBP. *Gene* 263: 131–140

Zimmermann L, Stephens A, Nam S-Z, Rau D, Kübler J, Lozajic M, Gabler F, Söding J, Lupas AN, Alva V (2018) A completely reimplemented MPI bioinformatics toolkit with a new HHpred server at its core. *J Mol Biol* 430: 2237–2243